

Matrix Difference in Pose-Graph Optimization

Irvin Aloise and Giorgio Grisetti

Abstract—Pose-Graph optimization is a crucial component of many modern SLAM systems. Most prominent state of the art systems address this problem by iterative non-linear least squares. Both number of iterations and convergence basin of these approaches depend on the error functions used to describe the problem. The smoother and more convex the error function with respect to perturbations of the state variables, the better the least-squares solver will perform.

In this paper we propose an alternative error function obtained by removing some non-linearities from the standard used one - i.e. the geodesic error function. Comparative experiments conducted on common benchmarking datasets confirm that our function is more robust to noise that affects the rotational component of the pose measurements and, thus, exhibits a larger convergence basin than the geodesic. Furthermore, its implementation is relatively easy compared to the geodesic distance. This property leads to rather simple derivatives and nice numerical properties of the Jacobians resulting from the effective computation of the quadratic approximation used by Gauss-Newton algorithm.

I. INTRODUCTION

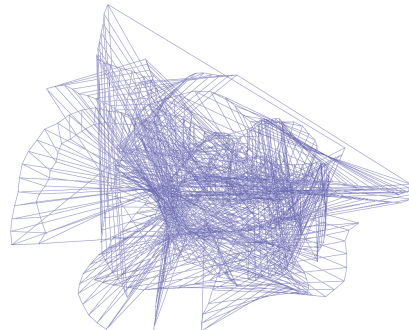
Simultaneous Localization and Mapping (SLAM) is a well known problem that has been studied intensively by the research community over the last two decades. Many paradigms have been proposed through the years to efficiently solve this problem. Amongst them, the *graph-based* approach gained much popularity in the last decade thanks to its efficiency and flexibility.

Graph-based SLAM approaches have generally two main components: a front-end whose role is to construct an abstract pose-graph from raw measurement data, and a back-end that has the task to provide the front-end and potentially other modules with an up-to-date consistent configuration of the pose-graph. For a detailed overview on this paradigm, we refer the reader to the work of Grisetti *et al.* [9].

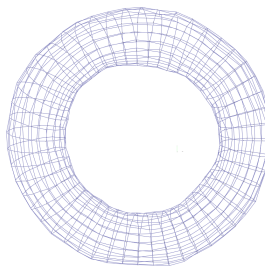
A pose-graph is a representation of a stochastic map. Its nodes represent samples of the robot trajectory or locations of local maps. Edges represent spatial constraints between local maps that can be inferred from measurements. As the robot travels, the graph is augmented by adding new nodes and edges, and its configuration might become inconsistent.

The task of the back-end is to constantly provide a consistent configuration of the pose-graph. The problem of graph optimization has been deeply investigated by the community in the recent years and effective systems are available. Nowadays, state-of-the-art back-ends are iterative solvers based on least-squares optimization [1] [16] [4].

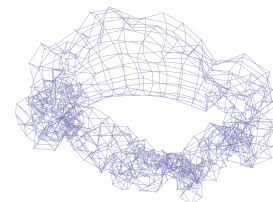
All authors are with the Department of Computer, Control, and Management Engineering Antonio Ruberti, Sapienza University of Rome, Rome, Italy, Email: ialoise@diag.uniroma1.it, grisetti@diag.uniroma1.it



(a) Initial guess from the spanning tree.



(b) Our approach.



(c) Geodesic distance.

Fig. 1: Result of optimization on the `torus-b` using Levenberg-Marquardt algorithm - 100 iterations. We perturbed the dataset with noise $\Sigma_R = [0.1 \ 0.1 \ 0.1]$ and $\Sigma_t = [0.001 \ 0.001 \ 0.001]$ - added respectively on the rotational and translational part of the pose. Optimization using the geodesic distance leads to a local minimum, while our approach succeeds in finding the right nodes configuration.

These solvers require that the current estimate is reasonably close to the optimum, assumption generally verified while running SLAM incrementally. Least-squares solvers operate by iteratively solving a quadratic approximation of the original minimization problem. A better approximation results in both a larger convergence basin and in faster convergence. However, the objective function for pose-to-pose edges in a pose graph is highly non-linear, especially in the 3D case, due to the presence of rotations.

To deal with this problem, Carlone *et al.* [2] proposed an approach to for solving 2D pose-graphs that constructs an exact quadratic approximation of the original problem by means of “unwinding” the angular component of the pose differences to avoid singularities. Such a solution is reported to provide good results when dealing with spherical covariances.

However such approach cannot be easily adapted to the three dimensional case. To this extent in a recent work Carlone *et al.* [3] addressed the crucial issue of finding a good initial guess for 3D pose-graph optimization. Determining a good initial guess is crucial when the system is started from

an unknown configuration of the poses - e.g. when operating on unorganized data. However, in case of on-line SLAM a reasonable solution is typically available. Still, in all cases the problem is turned to a non-linear optimization. A pose-graph is a particular case of a factor graph where the edges represent binary factors.

Several publicly available tools are commonly used to solve factor graphs such as GT-SAM [4], Ceres-Solver [1] and g^2o [16]. To use these tools one needs just to describe the domain of the state variables (nodes) and how to compute the errors induced by the measurements (factors) used in the problem. The additive nature of the factors allows the user to compose multiple heterogeneous measurements in a single factor graph.

In this work we propose a different error function to model pose-to-pose measurements that exhibits a smoother behavior compared to the commonly used geodesic distance. Its main features are:

- enlarged basin of convergence and, as a consequence, increased robustness of the optimization process
- simpler derivatives - compared the geodesic distance - that can be easily computed in closed form.

As illustrated in Fig. 1, our approach succeeds in finding the optimal nodes configuration in cases where the geodesic function remains stuck in local minimum. Moreover, when measurements are affected by realistic noise, the optimum obtained with our approach is equivalent to the one retrieved with the geodesic distance. Our claims are supported by comparative experiments on publicly available datasets. In addition to that, we provide an open source plugin¹ for g^2o that implements our error function, allowing to reproduce all the proposed experiments. In addition to that, we provide an Octave implementation of a simple least squares system, which is used to teach a SLAM course at Sapienza University of Rome.

II. RELATED WORK

The work of Lu and Milios [17] defined the graph-SLAM techniques in the context of laser scans. In this work they construct a pose-graph where each node represents a robot pose and the laser scan acquired at that pose. Edges were obtained either by odometry or by registering scans that were acquired at nearby poses. To optimize such a pose-graph they employed Gauss-Newton and treated the 2D poses as 3D Euclidean vectors, handling the singularities arising from angular difference in an ad-hoc manner. In the solution of the linear problem within least squares, the authors disregarded the sparse nature of the resulting linear system. This was not seen as an issue, since the number of scans considered and, thus, the size of the linear system was rather small, however as the size of the problem increases the solution of the linear system quickly become a computational bottleneck.

Gutmann and Konolidge [11] addressed the problem of incrementally building a map, finding topological relations

and loop closures based on local maps, and triggering the optimization only when the current state of the graph becomes substantially inconsistent. To avoid unnecessary computation they restricted the optimization to the sole portion of the graph that was reported as inconsistent, thus trading off computation and optimality of the solution.

To approach the computational issues in least-squares optimization Howard *et. al* [13] and Duckett *et. al.* [6] introduced relaxation. This approach is reported to be easy to implement, however its convergence rate is linear instead of quadratic. Compared to least squares approaches, each iteration is faster but more iterations are required to find the optimum. Frese *et. al.* proposed to use multilevel relaxation [7] to increase the convergence speed of the method.

Olson *et. al.* [19], proposed to use *Stochastic Gradient Descent* instead of least squares for 2D environments. Subsequently, this work was extended by Grisetti *et. al.* [10] addressing the 3D case and the introduction of a tree-based parameterization for the problem that further increased the convergence speed. However this work assumes that the measurements covariances are spherical and, therefore, this approach is not general.

Dallaert *et. al.* [5] released a system known as \sqrt{SAM} that exploited the sparsity of the linear system to efficiently compute a solution. In the same line, Kaess *et. al.* proposed iSAM [15] and iSAM2 [14]. These two works leverage on \sqrt{SAM} , adding respectively the features of incremental optimization and new data structures to the original system configuration. In parallel Kümmerle *et. al.* proposed g^2o [16], an optimization tool designed to easily prototype sparse least-squares solvers for factor graphs. g^2o builds on concepts from operating system realizing a layered structure that separates the problem definition from the problem solution and implements a plugin architecture that allows to modify most of its components. This allows the user to apply heterogeneous strategies to solve the factor graph, and to extend the types of “factors” and “node variables” upon need.

To further address the issues of poor initial guess and scalability, Ni *et. al* [18] and subsequently Grisetti *et. al* [8] applied divide and conquer strategies to find the optimal solution. The first approach leverages on nested dissection to solve the linear system, while the latter assembles a set of non-linear sparser problems from local portions of the graph.

When used to solve pose-graphs all those approaches suffer from the non-linearities introduced by the rotational component of the problem, leading to weak convergence results when the initial guess has a noisy rotational part. Notably, Carlone *et. al.* investigated this issue [3], proposing to relax the rotational constraints using different distance, generating a better initial guess for the standard optimization.

In this paper we propose an error function for pose-to-pose constraints that improves the stability of the optimization process that can be used in arbitrary pose-graphs. The proposed function is relatively easy to implement and has nice numerical properties. Our contribution is orthogonal to all least-squares methods mentioned above and can be used in conjunction with them.

¹Source code: https://srrg.gitlab.io/g2o_chordal_plugin.html

III. POSE GRAPHS OPTIMIZATION

In this section we quickly review some concepts on non-linear optimization for pose graphs. To deal with the non-Euclidean objects such as the isometries in the factor graph we rely on the manifold encapsulation technique proposed by Hertzberg *et. al* [12]. We furthermore discuss the effect of non-euclidean domains when evaluating the error function.

As stated in the introduction, the pose-graph is a graph whose nodes represent robot poses and edges represent relative transformations between poses. Let $\mathbf{X} = \mathbf{X}_{1:N}$ be the nodes in the graph, represented as 2D or 3D isometries, and let $\{(\mathbf{Z}_{ij}, \mathbf{\Omega}_{ij})\}$ be the edges in the graph with the subscript indicating the connected nodes. To capture the stochastic nature of the measurement to an edge we store not only the isometry \mathbf{Z}_{ij} that represents the measured relative location between nodes i and j , but also an information matrix $\mathbf{\Omega}_{ij}$ that captures the measurement's uncertainty along the different dimensions.

Pose-graph optimization consists in finding the configuration \mathbf{X}^* of nodes that minimizes the following objective function

$$\mathbf{X}^* = \underset{\mathbf{x}}{\operatorname{argmin}} \sum_{i,j} \|\mathbf{e}_{ij}(\mathbf{X}_i, \mathbf{X}_j)\|_{\mathbf{\Omega}_{ij}} \quad (1)$$

Here $\mathbf{e}_{ij}(\mathbf{X}_i, \mathbf{X}_j)$ is a vector function that measures the difference between the predicted measurement $\hat{\mathbf{Z}}_{ij} = \mathbf{h}(\mathbf{X}_i, \mathbf{X}_j) = \mathbf{X}_j \ominus \mathbf{X}_i$ and the measurement \mathbf{Z}_{ij} . With \ominus we refer to the motion decomposition operator as introduced in [20]. Assuming all variables are vectors, a straightforward implementation of the error function is thus the following:

$$\mathbf{e}_{ij}(\check{\mathbf{X}}) = \mathbf{h}(\check{\mathbf{X}}_i, \check{\mathbf{X}}_j) - \mathbf{Z}_{ij}. \quad (2)$$

Eq. (1) is usually solved by iterative non-linear least squares minimization, leading to the popular Gauss-Newton or Levenberg-Marquardt methods. We refer the reader to [9] for a comprehensive tutorial on least-squares on pose-graphs. The core idea of these methods is to repeatedly refine a current initial guess of the solution $\check{\mathbf{X}}$ by solving many times its quadratic approximation. The latter is obtained through the first-order Taylor expansion of the error function evaluated around $\check{\mathbf{X}}$:

$$\begin{aligned} \mathbf{e}_{ij}(\check{\mathbf{X}} + \Delta\mathbf{X}) &= \mathbf{h}(\check{\mathbf{X}}_i + \Delta\mathbf{X}_i, \check{\mathbf{X}}_j + \Delta\mathbf{X}_j) - \mathbf{Z}_{ij} \quad (3) \\ &\approx \mathbf{e}_{ij}(\check{\mathbf{X}}) + \left. \frac{\partial \mathbf{h}_{ij}(\mathbf{X}_i, \check{\mathbf{X}}_j)}{\partial \mathbf{X}_i} \right|_{\mathbf{x}_i=\check{\mathbf{x}}_i} \Delta\mathbf{X}_i + \\ &\quad + \left. \frac{\partial \mathbf{h}_{ij}(\check{\mathbf{X}}_i, \mathbf{X}_j)}{\partial \mathbf{X}_j} \right|_{\mathbf{x}_j=\check{\mathbf{x}}_j} \Delta\mathbf{X}_j \end{aligned}$$

A. Smooth Manifolds Encapsulation

The above operation leverages on the correct definition of vector subtraction and addition, and assumes that both states \mathbf{X} and measurements \mathbf{Z} live in Euclidean spaces. In case of pose graphs, however this is no longer the case since isometries lie on smooth manifolds $SE(2)$ and $SE(3)$

respectively. A manifold is a space that, albeit non homeomorphic to \mathbb{R}^n , admits a locally Euclidean parametrization around each element \mathbf{M} of the domain, commonly referred to as *chart*. Therefore, a chart computed around a manifold point \mathbf{M} is a function from \mathbb{R}^n to a new point \mathbf{M}' on the manifold:

$$\operatorname{chart}_{\mathbf{M}}(\Delta\mathbf{m}) : \mathbb{R}^n \rightarrow \mathbf{M}. \quad (4)$$

Intuitively, \mathbf{M}' is obtained by ‘‘walking’’ along the perturbation $\Delta\mathbf{m}$ on the chart, starting from the chart origin. A null motion ($\Delta\mathbf{m} = \mathbf{0}$) on the chart, leaves us at the point where the chart is constructed: $\operatorname{chart}_{\mathbf{M}}(\mathbf{0}) = \mathbf{M}$.

Similarly, given two points \mathbf{M} and \mathbf{M}' on the manifold, we can determine the motion $\Delta\mathbf{m}$ on the chart constructed around \mathbf{M} that would bring us to \mathbf{M}' . Let this operation be the inverse $\operatorname{chart}_{\mathbf{M}}^{-1}(\mathbf{M}')$. The direct and inverse charts allow us to define operators on the manifold that are analogous to the sum and subtraction in the Euclidean space. Let \boxplus and \boxminus be those operators, defined as follows:

$$\mathbf{M} \boxplus \Delta\mathbf{m} \triangleq \operatorname{chart}_{\mathbf{M}}(\Delta\mathbf{m}) \quad (5)$$

$$\mathbf{M}' \boxminus \mathbf{M} \triangleq \operatorname{chart}_{\mathbf{M}}^{-1}(\mathbf{M}') \quad (6)$$

This notation was first introduced by Hertzberg and Frese [12], and allows us to easily adapt the Euclidean version of non-linear Least-Squares to operate on manifold spaces. The parameterization of the chart is usually chosen to be of minimal dimension, while the representation of the manifold element \mathbf{M} can be chosen arbitrarily. Accordingly, two possible parametrizations for $SE(3)$ objects are:

$$\mathbf{X} = \begin{pmatrix} \mathbf{R} & \mathbf{t} \\ \mathbf{0}_{3 \times 1} & 1 \end{pmatrix} \quad \mathbf{R} = \mathbf{R}_x(\phi) \mathbf{R}_x(\theta) \mathbf{R}_x(\psi) \quad (7)$$

$$\Delta\mathbf{x} = (x \ y \ z \ \phi \ \theta \ \psi)^T \quad (8)$$

Accordingly, to compute the difference between two isometries or to apply an increment to an isometry, we need to define the operators \boxminus and \boxplus . In the remainder of this section, we will use the following definition for such operators:

$$\mathbf{X} \boxplus \Delta\mathbf{x} = \mathbf{v}2\mathbf{t}(\Delta\mathbf{x})\mathbf{X} \quad (9)$$

$$\mathbf{X}_a \boxminus \mathbf{X}_b = \mathbf{t}2\mathbf{v}(\mathbf{X}_b^{-1}\mathbf{X}_a) \quad (10)$$

Here $\mathbf{t}2\mathbf{v}$ and $\mathbf{v}2\mathbf{t}$ map an isometry into a 6D minimal vector and vice-versa. We refer the reader to Appendix I for the mathematical definitions of these functions. Hence, we can compute the error between predicted and actual measurement as $\mathbf{e}_{ij} = \hat{\mathbf{Z}}_{ij} \boxminus \mathbf{Z}_{ij}$. To minimize the objective function in Eq. (1) using an iterative approach we need to compute its Taylor approximation around the current estimate $\check{\mathbf{X}}$. Setting $\mathbf{e}_{ij} = \mathbf{e}_{ij}(\check{\mathbf{X}})$ and expressing the perturbation on the charts

results in the following expansion:

$$\mathbf{e}_{ij}(\check{\mathbf{X}} \boxplus \Delta \mathbf{x}) = \mathbf{h}_{ij}(\check{\mathbf{X}}_i \boxplus \Delta \mathbf{x}_i, \check{\mathbf{X}}_j \boxplus \Delta \mathbf{x}_j) \boxminus \mathbf{Z}_{ij} \quad (11)$$

$$\approx \mathbf{e}_{ij} + \underbrace{\frac{\partial \mathbf{e}_{ij}(\check{\mathbf{X}}_i \boxplus \Delta \mathbf{x}_i, \check{\mathbf{X}}_j)}{\partial \Delta \mathbf{x}_i}}_{\tilde{\mathbf{J}}_i} \Big|_{\Delta \mathbf{x}_i=0} \Delta \mathbf{x}_i + \quad (12)$$

$$+ \underbrace{\frac{\partial \mathbf{e}_{ij}(\check{\mathbf{X}}_i, \check{\mathbf{X}}_j \boxplus \Delta \mathbf{x}_j)}{\partial \Delta \mathbf{x}_j}}_{\tilde{\mathbf{J}}_j} \Big|_{\Delta \mathbf{x}_j=0} \Delta \mathbf{x}_j \quad (13)$$

The smoother the function $\mathbf{e}_{ij}(\cdot)$ with respect to the perturbation, the better the final quadratic form will approximate the nonlinear problem. This results both in less iterations and larger convergence basin. To the limit, if the Jacobians are not affected by the linearization point one can find the solution in just one iteration. In Eq. (11) we explicitly addressed the fact that only the blocks $\Delta \mathbf{x}_i$ and $\Delta \mathbf{x}_j$ in the perturbation vector $\Delta \mathbf{x} = \Delta \mathbf{x}_{1:N}$ determine the error between nodes i and j . The full jacobian with respect to all perturbation blocks has the following general structure:

$$\tilde{\mathbf{J}}_{ij} = [0 \cdots 0 \mathbf{J}_i 0 \cdots 0 \mathbf{J}_j 0 \cdots 0]. \quad (14)$$

B. Error on a Chart

Comparing equations Eq. (2) and Eq. (11), the reader might notice that the subtraction between prediction $\hat{\mathbf{Z}}_{ij} = \mathbf{h}(\mathbf{X}_i, \mathbf{X}_j)$ and observation \mathbf{Z}_{ij} has been replaced by a \boxminus operator. This is coherent with the fact that the measurement \mathbf{Z}_{ij} and the prediction \mathbf{h}_{ij} are manifolds. This, however, introduces an additional nonlinear transformation in the calculation of the omega-norm. Intuitively, since the error is computed on a chart constructed around the measurement, the value of the error on the chart needs to be reestimated each time the prediction changes. This is consistent with the fact that the original information matrix of the measurement Ω_{ij} has dimensions consistent with the measurement \mathbf{Z}_{ij} , which might be different from the ones of the error vector \mathbf{e}_{ij} . This can be solved by computing a Gaussian approximation of the error distribution around the manifold measurement: given the relations $\mathbf{z} = \text{t2v}(\mathbf{Z})$ and $\mathbf{z}_{ij} = \text{t2v}(\mathbf{Z}_{ij})$ we can write:

$$p(\mathbf{z}) \sim \mathcal{N}(\mathbf{z}_{ij}, \Omega_{ij}^{-1}) \quad (15)$$

$$\mathbf{e}_{ij} = \hat{\mathbf{Z}}_{ij} \boxminus \mathbf{Z} \quad (16)$$

$$p(\mathbf{e}_{ij}) \sim \mathcal{N}(\hat{\mathbf{Z}}_{ij} \boxminus \mathbf{Z}_{ij}, \mathbf{J}_{\mathbf{Z}_{ij}} \Omega_{ij}^{-1} \mathbf{J}_{\mathbf{Z}_{ij}}^T) \quad (17)$$

$$\text{with } \mathbf{J}_{\mathbf{Z}_{ij}} = \frac{\partial (\hat{\mathbf{Z}}_{ij} \boxminus \mathbf{Z})}{\partial \mathbf{z}} \Big|_{\mathbf{z}=\mathbf{z}_{ij}} \quad (18)$$

The reader might notice that $\mathbf{J}_{\mathbf{Z}_{ij}}$ depends on the prediction and, thus, on the linearization point. Accordingly, the covariance of the error $\tilde{\Omega}_{ij}^{-1} = \mathbf{J}_{\mathbf{Z}_{ij}} \Omega_{ij}^{-1} \mathbf{J}_{\mathbf{Z}_{ij}}^T$ is a function of the state and should be recomputed at each iteration. However, when using the same representation for the error vector and the perturbations, and when the prediction and the measurement are close we have that the Jacobian $\mathbf{J}_{\mathbf{Z}_{ij}} \approx \mathbf{I}$ and many state-of-the-art systems simply ignore this step.

Algorithm 1 Gauss-Newton minimization algorithm for manifold measurements and state spaces

Require: Initial guess $\check{\mathbf{X}}$; Measurements $\mathcal{C} = \{\langle \mathbf{Z}_k, \Omega_k \rangle\}$

Ensure: Optimal solution \mathbf{X}^*

```

1:  $F_{new} \leftarrow \check{F}$  ▷ compute the current error
2: while  $\check{F} - F_{new} > \epsilon$  do
3:    $\check{F} \leftarrow F_{new}$ 
4:    $\mathbf{b} \leftarrow 0$ 
5:    $\mathbf{H} \leftarrow 0$ 
6:   for  $\mathbf{Z}_{ij} \in \mathcal{C}$  do
7:      $\hat{\mathbf{Z}}_{ij} \leftarrow \mathbf{h}_{ij}(\check{\mathbf{X}})$  ▷ compute prediction
8:      $\mathbf{e}_{ij} \leftarrow \hat{\mathbf{Z}}_{ij} \boxminus \mathbf{Z}_{ij}$  ▷ compute the error
9:      $\tilde{\mathbf{J}}_{ij} \leftarrow \frac{\partial \mathbf{e}_{ij}(\mathbf{h}_k(\check{\mathbf{X}} \boxplus \Delta \mathbf{x}), \mathbf{z}_k)}{\partial \Delta \mathbf{x}_k} \Big|_{\Delta \mathbf{x}_k=0}$  ▷ jac of  $\boxminus$ 
10:     $\mathbf{J}_{\mathbf{Z}_{ij}} \frac{\partial (\hat{\mathbf{Z}}_{ij} \boxminus \mathbf{Z})}{\partial \mathbf{Z}} \Big|_{\mathbf{Z}=\mathbf{Z}_{ij}}$  ▷ error jac. on the chart
11:     $\tilde{\Omega}_k \leftarrow (\mathbf{J}_{\mathbf{Z}_k} \Omega_k \mathbf{J}_{\mathbf{Z}_k}^T)^{-1}$  ▷ remap Omega
12:     $\mathbf{H}_k \leftarrow \mathbf{J}_{\mathbf{Z}_k}^T \tilde{\Omega}_k \mathbf{J}_{\mathbf{Z}_k}$  ▷ contribution of  $\mathbf{Z}_{ij}$  in  $\mathbf{H}$ 
13:     $\mathbf{b}_k \leftarrow \mathbf{J}_{\mathbf{Z}_k}^T \tilde{\Omega}_k \mathbf{e}_k$  ▷ contribution of  $\mathbf{Z}_{ij}$  in  $\mathbf{b}$ 
14:     $\mathbf{H} += \mathbf{H}_k$  ▷ accumulate contributions
15:     $\mathbf{b} += \mathbf{b}_k$  ▷ accumulate contributions
16:    $\Delta \mathbf{x} \leftarrow \text{solve}(\mathbf{H} \Delta \mathbf{x} = -\mathbf{b})$  ▷ solve w.r.t.  $\Delta \mathbf{x}$ 
17:    $\check{\mathbf{X}} \leftarrow \check{\mathbf{X}} \boxplus \Delta \mathbf{x}$  ▷ update the state
18:    $F_{new} \leftarrow F(\check{\mathbf{X}})$  ▷ compute the new error
19: return  $\check{\mathbf{X}}$ 

```

C. Gauss-Newton for Pose Graphs on a Manifold

For sake of completeness, in this section we report an algorithmic presentation of the minimization algorithm that combines all the elements sketched in the previous sections. Alg. 1 reports the pseudo-code of such optimization process.

The quadratic form is obtained by expanding the Taylor approximation in the summands of Eq. (1) as follows:

$$\begin{aligned} \mathbf{F}_{ij}(\check{\mathbf{X}} \boxplus \Delta \mathbf{x}) &= \|\mathbf{e}_{ij}(\check{\mathbf{X}} \boxplus \Delta \mathbf{x})\|_{\tilde{\Omega}_{ij}} \\ &\approx (\mathbf{e}_{ij} + \mathbf{J}_{ij} \Delta \mathbf{x})^T \tilde{\Omega}_{ij} (\mathbf{e}_{ij} + \mathbf{J}_{ij} \Delta \mathbf{x}) = \\ &= \Delta \mathbf{x}^T \underbrace{\tilde{\mathbf{J}}_{ij}^T \tilde{\Omega}_{ij} \tilde{\mathbf{J}}_{ij}}_{\mathbf{H}_{ij}} \Delta \mathbf{x} + 2 \underbrace{\mathbf{e}_{ij}^T \tilde{\Omega}_{ij} \tilde{\mathbf{J}}_{ij}}_{\mathbf{b}_{ij}} \Delta \mathbf{x} + \underbrace{\mathbf{e}_{ij}^T \tilde{\Omega}_{ij} \mathbf{e}_{ij}}_{\mathbf{c}_{ij}} \end{aligned} \quad (19)$$

Considering all the measurements, the global cost around $\check{\mathbf{X}}$ as a function of the perturbation function will be:

$$\begin{aligned} \mathbf{F}(\check{\mathbf{X}} \boxplus \Delta \mathbf{x}) &= \sum_{\mathbf{Z}_{ij} \in \mathcal{C}} \mathbf{F}_{ij}(\check{\mathbf{X}} \boxplus \Delta \mathbf{x}) \\ &\approx \Delta \mathbf{x}^T \mathbf{H} \Delta \mathbf{x} + 2 \mathbf{b} \Delta \mathbf{x} + \mathbf{c} \end{aligned} \quad (20)$$

We can find the minimum of Eq. (20) computing its derivative and equating it to 0. This means that we have to solve the following linear system w.r.t. $\Delta \mathbf{x}$

$$\mathbf{H} \Delta \mathbf{x} = -\mathbf{b} \quad (21)$$

The result will be an increment $\Delta \mathbf{x}$ that applied to $\check{\mathbf{X}}$ will lead to a state closer to the optimal one:

$$\mathbf{X} \leftarrow \check{\mathbf{X}} \boxplus \Delta \mathbf{x} \quad (22)$$

Iterative algorithms repeat this process until convergence is reached.

IV. POSE ERROR FUNCTIONS

In this section, we analyze in depth a typical error function used in pose-graph optimization, and we will focus on the 3D case. The extension to 2D pose graphs is straightforward.

A. Standard SE3 Error

A standard way of computing the pose-pose error uses the operator \boxplus and \boxminus defined in Eq. (9) and Eq. (10). Following this formalization and embedding the perturbations together with the \boxplus operator, we can compute the perturbed error as:

$$\begin{aligned} \mathbf{e}_{ij}(\mathbf{X}_i \boxplus \Delta \mathbf{x}_i, \mathbf{X}_j \boxplus \Delta \mathbf{x}_j) = \\ = \mathbf{t}2\mathbf{v} \left(\mathbf{Z}_{ij}^{-1} (\mathbf{v}2\mathbf{t}(\Delta \mathbf{x}_i) \mathbf{X}_i)^{-1} (\mathbf{v}2\mathbf{t}(\Delta \mathbf{x}_j) \mathbf{X}_j) \right) \end{aligned} \quad (23)$$

Eq. (23) is highly non-linear and it suffers from a large number of singularities, mainly due to the use of function $\mathbf{t}2\mathbf{v}$ that converts a transformation matrix in a minimal representation - refer to Appendix I. Therefore, it propagates such non-linearities in the Jacobians and, thus, to the whole optimization process.

B. Chordal-Based SE3 Error

As mentioned in [3], we can define an alternative error function based on the concept of *chordal distance*. To this end, we first introduce the function $\text{flatten}(\cdot)$, defined as follows:

$$\text{flatten}(\mathbf{T}) = (\mathbf{r}_1^T \quad \mathbf{r}_2^T \quad \mathbf{r}_3^T \quad \mathbf{t}^T)^T \quad (24)$$

where \mathbf{r}_j represents the j -th versor of the rotation matrix \mathbf{R} . Basically, it is a linear transformation that reshapes an isometry into the 12D-vector containing rotation vector and translation. According to this, we define new \boxplus and \boxminus operators as follows:

$$\mathbf{X} \boxplus \Delta \mathbf{x} = \mathbf{v}2\mathbf{t}(\Delta \mathbf{x})\mathbf{X} \quad (25)$$

$$\mathbf{X}_a \boxminus \mathbf{X}_b = \text{flatten}(\mathbf{X}_a) - \text{flatten}(\mathbf{X}_b) \quad (26)$$

It is important to notice that in Eq. (26), the difference is done through the standard Euclidean minus operator. As a result, the 12-dimensional error between two $SE(3)$ becomes:

$$\mathbf{e}_{ij} = \hat{\mathbf{Z}}_{ij} \boxminus \mathbf{Z}_{ij} = \text{flatten}(\mathbf{X}_i^{-1}\mathbf{X}_j) - \text{flatten}(\mathbf{Z}_{ij}) \quad (27)$$

Note that, in this sense, we use two different parametrizations for the error and increments. The derivation of Jacobians \mathbf{J}_i and \mathbf{J}_j from Eq. (27) is reported in Appendix I. Eliminating $\mathbf{t}2\mathbf{v}$ from Eq. (23) removes substantial non-linearities and, thus, produces a smoother function. This leads to an enlarged convergence basin, increasing the robustness of the optimization process with respect to noise. Finally, we observe that the two Jacobians are linked by the relation $\mathbf{J}_i = -\mathbf{J}_j$, as reported in Appendix I. Accordingly, the four contributions to \mathbf{H} introduced by measurement \mathbf{Z}_{ij} will be:

$$\mathbf{H}_{ii} = \mathbf{H}_{jj} = -\mathbf{H}_{ij} = -\mathbf{H}_{ji} = \mathbf{J}_i^T \mathbf{\Omega}_{ij} \mathbf{J}_j \quad (28)$$

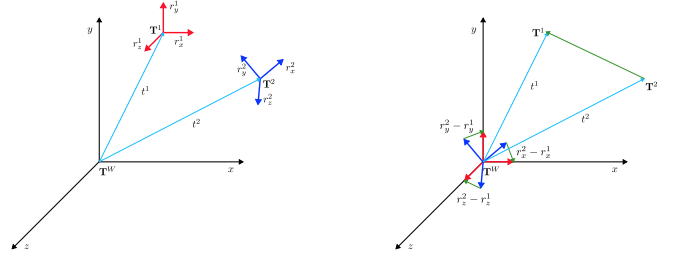


Fig. 2: In this figure we show the principle behind our $SE(3)$ error function. The leftmost illustration depicts two poses \mathbf{T}_1 and \mathbf{T}_2 . Supposing that we want to compute $d_{chord}(\mathbf{T}_1, \mathbf{T}_2)$, the rightmost illustration visually shows how this is computed: the translational part is simply $\mathbf{t}_2 - \mathbf{t}_1$ as usual; the rotational part is computed as the difference between the versors of the two rotations - namely $\mathbf{r}_j^2 - \mathbf{r}_j^1$ with $j = \{x, y, z\}$

The consequences of Eq. (28) are rather substantial in the computation of the \mathbf{H} matrix. In one single operation we can compute all four entries of \mathbf{H} that are affected by a measurement, and this leverages the cost of operating with twelve instead of six dimensional error vectors. Notably, Eq. (27) uses a vector difference instead of the non-linear $\mathbf{t}2\mathbf{v}$, therefore the information matrix $\hat{\mathbf{\Omega}}_{ij}$ does not need to be recomputed at each iteration. This has the dual effect of speeding up the computation and leading to a more consistent quadratic approximation of the problem.

Usually, the input problem expresses the measurements through a minimal six-dimensional parameterization such as translation and normalized quaternion or translation and Euler angles. Therefore, we cannot reuse these information matrices as they are, but we need to transform them to the new representation that has 12 parameters. This can be done using either first order error propagation or with the Unscented Transform. Mapping a 6 dimensional Gaussian onto a 12 dimensional space will unavoidably lead to a non positive definite covariance matrix due to the inherent rank losses. We solve this problem adding a small $\epsilon > 0$ to the null singular values of the covariance matrix before inverting it to obtain the 12D information matrix. We verified this procedure by performing the inverse transformation (12D to 6D) and by verifying that the restored problem has information matrices numerically close to those of the original one.

V. EXPERIMENTAL EVALUATION

In this section we investigate the effects the *chordal distance* error function presented in Section IV-B. We provide some key tests to support the claim that our error function leads to a larger convergence basin with respect to the one based on the geodesic distance. To this end, we tested the optimization on several standard pose-graph datasets, comparing the evolution of the optimization residual error employing the standard and the proposed error function. All tests have been conducted on 3-dimensional pose graphs. We tested our error function embedding it within the g^2o optimization framework. Datasets specifications are available in Fig. 3 and in Tab. I.

To evaluate the performances of approaches under varying noise conditions, we added to the original datasets noise sampled from $\mathcal{N}_t(0, \Sigma_t)$ and $\mathcal{N}_R(0, \Sigma_R)$ respectively for the

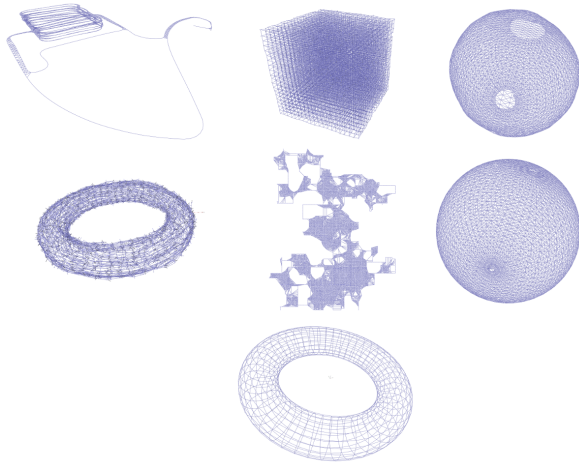


Fig. 3: Datasets used to perform the experiments. Top row, from left to right: pose graph of the Stanford parking garage (referred as *garage*), simulated 3D grid (*grid*), simulated 3D sphere (*sphere-a*); mid row, left to right: simulated 3D torus (*torus-a*), simulated 3D dataset (*sim-manhattan*), simulated 3D sphere (*sphere-b*); last row: simulated 3D torus (*torus-b*).

translational and rotational component of the pose. Then we analyzed the convergence using the chordal and the geodesic error functions, varying both the statistical parameters of the noise distributions and the initial guess. To compare the residual error evolution between the two error functions, we recompute the χ^2 - i.e. the quadratic error obtained summing the e_k computed for each measurement \mathbf{Z}_k - at each iteration of the chordal optimization using the geodesic function. In Section V-A we present the result obtained with spherical covariances. In Section V-B we report the effects of the optimization under generic covariances. Since the value of parameter ϵ controls the conversion between geodesic and chordal problem, we investigated the effects of this parameter in Section V-C.

A. Spherical Covariances

In the first set of experiments, we added a relatively small noise figure to the pose measurements. In particular, the statistical parameters are $\Sigma_t = [0.1 \ 0.1 \ 0.1][m]$ and $\Sigma_R = [0.01 \ 0.01 \ 0.01][rad]$. As shown in Fig. 4, both error function succeed in finding the optimum, although our approach requires slightly more iterations.

Then, we increased the noise using $\Sigma_t = [0.5 \ 0.5 \ 0.5][m]$ and $\Sigma_R = [0.1 \ 0.1 \ 0.1][rad]$. In this case the noise components are very high in each pose dimension. Results of the optimization process on the *sphere-a* dataset are shown in Fig. 5. These initial guesses are extremely poor,

Dataset	# Vert.	# Meas.
garage	1661	6275
grid	8000	22236
sphere-a	2200	8647
torus-a	5000	9048
sim-manhattan	5001	60946
sphere-b	2500	9799
torus-b	1000	1999

TABLE I: Specs of the datasets used for the experiments.

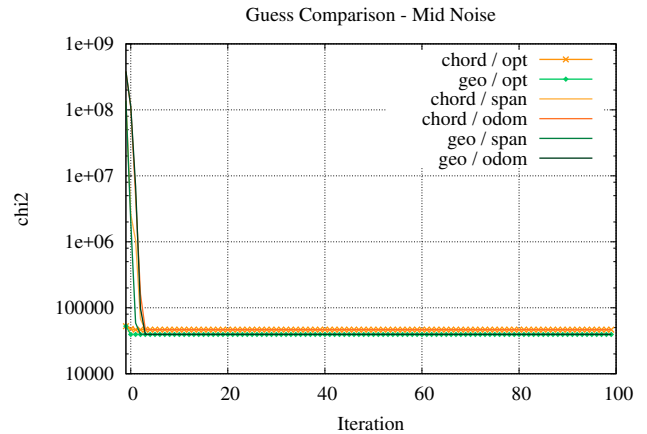


Fig. 4: Evolution of the χ^2 in dataset *sphere-a* with noise covariances $\Sigma_t = [0.1 \ 0.1 \ 0.1][m]$ and $\Sigma_R = [0.01 \ 0.01 \ 0.01][rad]$. Both approaches easily succeed.

and neither of the two approaches can reach the optimum. However, the chordal function produces better results with respect to the geodesic one.

B. Non-Spherical Covariances

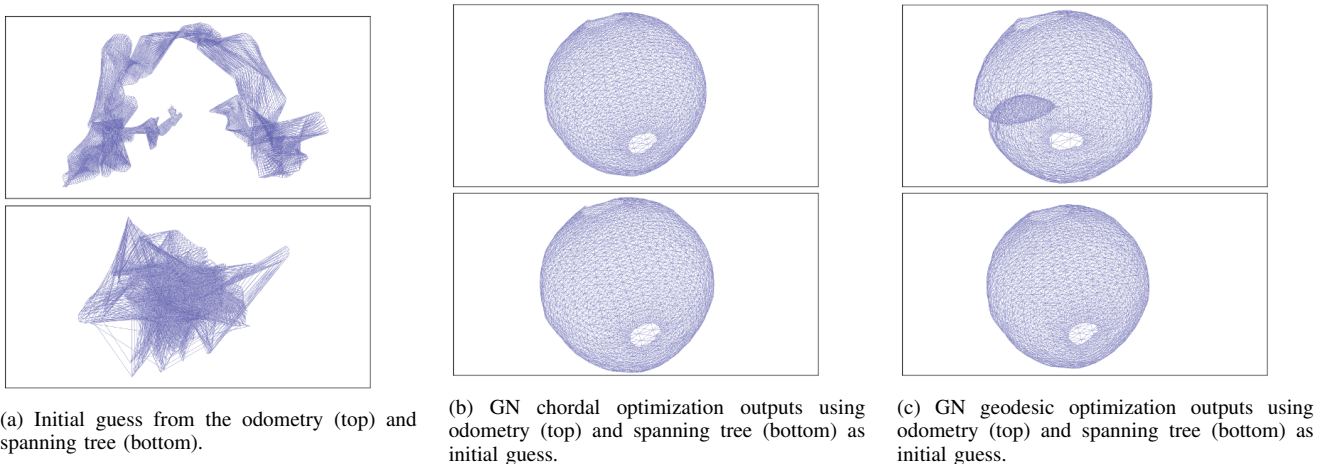
For the second set of experiments, we used $\Sigma_t = [0.5 \ 0.5 \ 0.01][m]$ and $\Sigma_R = [0.0001 \ 0.0001 \ 0.1][rad]$. With this noise figures, we want to investigate the effects of extremely non-spherical measurements covariance matrices in the optimization process. In this configuration our error function can reach the optimum even when the geodesic error function remains stuck in a local minimum or the linear system cannot be solved due to numerical issues. In Fig. 6 the reader can find the analysis of such case for the *sim-mahattan* dataset. The results obtained from the other datasets are consistent with *sim-mahattan*, and we omit them for sake of brevity.

We observed that when the rotational noise is particularly large - e.g. $\Sigma_R = [0.1 \ 0.1 \ 0.1]$ - using the geodesic error function for the optimization leads to solutions that are further from the optimum than the ones reported by our approach. Intuitively, large values of rotational noise tend to excite more the non-linearities in the error function, that are the main source of non-convexity.

In conclusion we observed that the proposed error function exhibits a larger convergence basin compared to the geodesic one while requiring a slightly higher number of iterations in order to reach the optimum.

C. Influence of Covariance Conversion on the Optimum

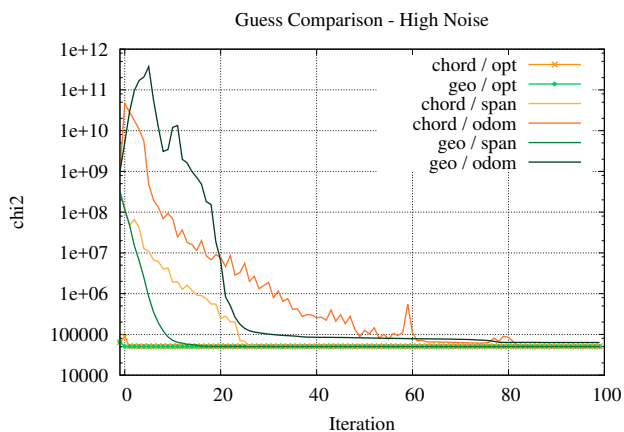
The reader might notice that in Fig. 6d, the two approaches converge to a slightly different optimum. This mismatch is due to the value ϵ used to convert the information matrix. The results reported for all experiments are obtained by using a value of $\epsilon = 0.1$. Using such a value has negligible effects on the minimum of the converted error problem when the measurements are affected by a standard deviation in the same order of magnitude as ϵ . In this case, the optimum of the geodesic and the chordal problems are equivalent in terms of χ^2 - e.g. as reported in Fig. 5d and Fig. 5e. However,



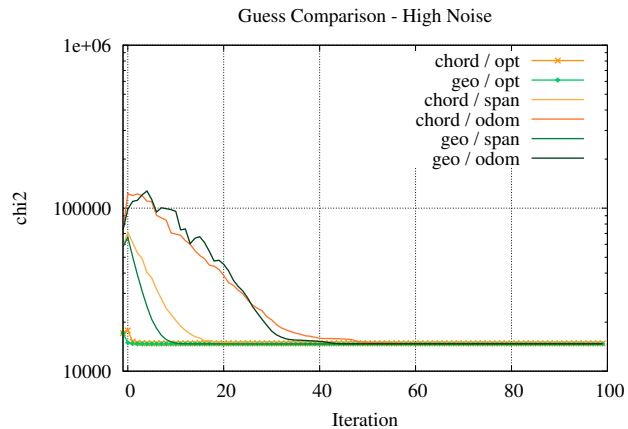
(a) Initial guess from the odometry (top) and spanning tree (bottom).

(b) GN chordal optimization outputs using odometry (top) and spanning tree (bottom) as initial guess.

(c) GN geodesic optimization outputs using odometry (top) and spanning tree (bottom) as initial guess.



(d) Comparison of the chi2 using Gauss-Newton as optimization algorithm.



(e) Comparison of the chi2 using Gauss-Newton and a Cauchy kernel with width $k = 1.0$.

Fig. 5: Analysis of the `sphere-a` synthetic dataset. We encoded in the measurements noise sampled from Gaussian distributions with $\Sigma_t = [0.5 \ 0.5 \ 0.5][m]$ and $\Sigma_R = [0.1 \ 0.1 \ 0.1][rad]$. The initial guesses computed from the odometry traversal and the spanning tree are reported in Fig. 5a. The output produced by the Gauss-Newton (GN) optimization using the chordal and the geodesic distances are illustrated respectively in Fig. 5b and Fig. 5c. Even in this case the geodesic distance remains stuck in a local minimum, as highlighted in Fig. 5d. Introducing a Cauchy kernel in the optimization process, both functions reach the same optimum as shown in Fig. 5e.

when ϵ is large compared to the noise in one or more dimensions, the two optima are in slightly different, albeit visual inspection of the pose graph reveal no substantial inconsistencies. This problem can be approached in two alternative ways:

- Start an optimization using the geodesic error function from the optimum obtained by using the chordal function. In general the chordal solution represents a very good starting point, and the geodesic error function converges in a few steps.
- Dynamically adapt the value of ϵ using an adaptive strategy based on the rate of convergence. This results in a strategy similar to the Levenberg-Marquardt algorithm.

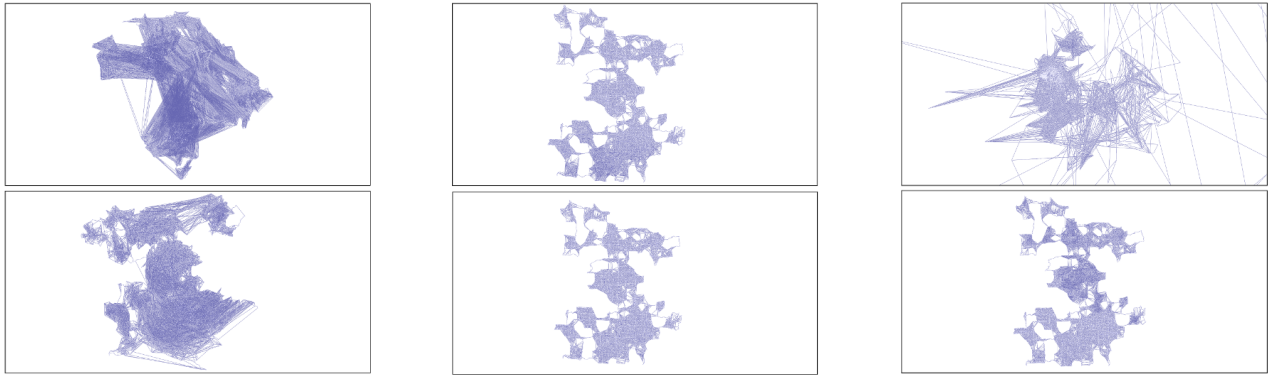
To characterize the influence of parameter ϵ in the optimization, we performed a third experiment. We perturbed the `sphere-a` dataset adding the following noise figures $\Sigma_t = [0.5 \ 0.5 \ 0.01][m]$ and $\Sigma_R = [0.0001 \ 0.0001 \ 0.1][rad]$. In Fig. 7 we reported the chi2 of different optimizations obtained varying the value of ϵ , using the optimum as initial guess. The experiments confirm our conjectures that ϵ values larger than the noise standard deviation - on one or more

dimensions - will smoothen the error surface leading to different optima with respect to the one retrieved with the geodesic distance.

VI. CONCLUSIONS

In this work we proposed an alternative error function for 3D pose-graph optimization problems, based on the chordal distance between matrices rather than the geodesic one. Its main features are: (i) reduction of problem's non-linearities with a consequent enlarged convergence basin and a greater robustness to rotational noise, (ii) derivatives easy to compute in close form and that lead to nice numerical properties of the Jacobians - e.g. one is the opposite of the other - and, thus, to a faster computation of matrix \mathbf{H} .

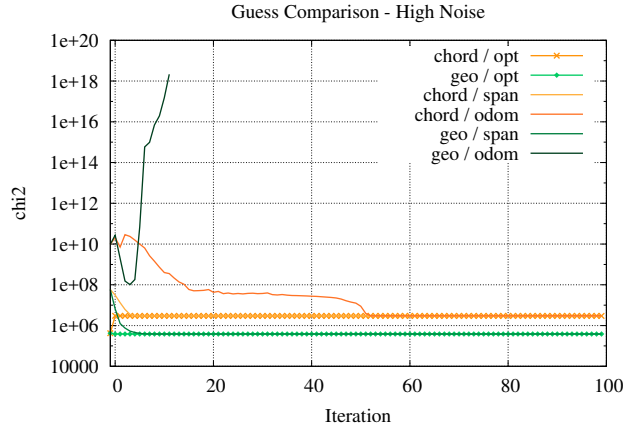
Our conjectures are confirmed by a large set of comparative experiments. To use the chordal error function, one has to convert the problem expressed in geodesic form. Under realistic conditions, the converted problem has a solution equivalent to the original one. Under extremely uneven noise figures the two optima might be different, however we by visual inspection we were not able to spot inconsistencies in the returned solutions.



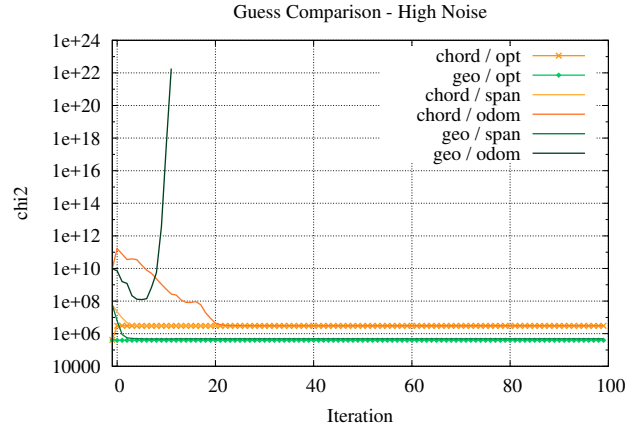
(a) Top: initial guess from odometry; bottom: initial guess from spanning tree

(b) GN chordal output from odometry (top) and from spanning tree (bottom).

(c) GN geodesic outputs from odometry (top) and from spanning tree (bottom).



(d) Comparison of the χ^2 using Gauss-Newton as optimization algorithm. If the initial guess is far from the optimum - e.g. odometry case - the geodesic error function stops the optimization before the end of the iterations due to numerical problems.



(e) Comparison of the χ^2 using Gauss-Newton and a Cauchy kernel with kernel width $k = 1.0$. When the initial guess is far from the optimum, the optimization stops before the end of the iterations using the geodesic distance.

Fig. 6: Analysis of the `sim-manhattan` dataset. We encoded in the measurements noise sampled from Gaussian distributions with $\Sigma_t = [0.5 \ 0.5 \ 0.01][m]$ and $\Sigma_R = [0.0001 \ 0.0001 \ 0.1][rad]$. With such noise, the initial guesses computed through odometry and spanning tree are reported in Fig. 6a. The results after 100 iterations of Gauss-Newton (GN) optimization using the chordal and the geodesic error function are depicted respectively in Fig. 6b and Fig. 6c. Using the standard error function, the optimization process will fail, due to numeric issue - i.e. Hessian non-PSD. Fig. 6d illustrates the residual error - i.e. the χ^2 - evolution over 100 iterations. Adding a Cauchy robust kernel to the geodesic optimization, the final state reached is not as far from the optimum as in the previous case, however the problem is still numerically unstable. Curves marked as `opt` in the legend show the optimization evolution using the optimum as initial guess, so they are used as reference for the two error functions.

APPENDIX I JACOBIANS' COMPUTATION

In this small Appendix we provide the mathematical derivation of the Jacobians both in the standard parametrization and in the chordal one.

a) *Standard Formalization*: Let \mathbf{X} be a 3D-isometry composed as in Eq. (7); let $\Delta \mathbf{x}$ be a 6-vector defined as in Eq. (8). The functions `v2t` and `t2v` map a 6-vector into a 3D-isometry and vice-versa. The former one ensembles the transformation as follows:

$$\mathbf{v2t}(\Delta \mathbf{x}) = \begin{pmatrix} \mathbf{R} & \mathbf{t} \\ \mathbf{0}_{3 \times 1} & 1 \end{pmatrix} \quad \mathbf{t} = [\Delta x \ \Delta y \ \Delta z]^T \quad (29)$$

$$\mathbf{R} = \mathbf{R}_x(\Delta \phi) \mathbf{R}_y(\Delta \theta) \mathbf{R}_z(\Delta \psi)$$

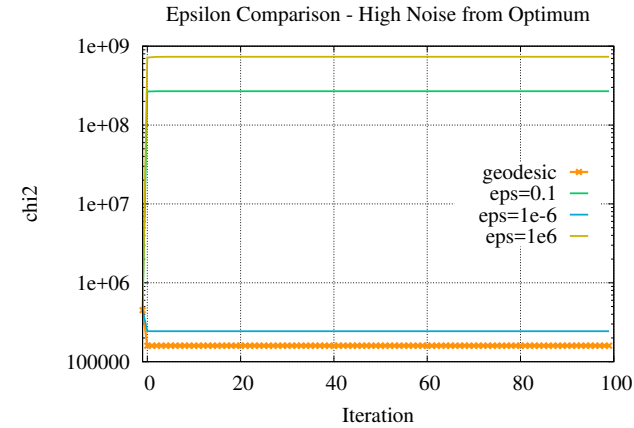


Fig. 7: Evolution of the χ^2 on the `sphere-a` dataset with noise statistics equal to $\Sigma_t = [0.5 \ 0.5 \ 0.01][m]$ and $\Sigma_R = [0.0001 \ 0.0001 \ 0.1][rad]$. The smaller ϵ , the closer the chordal optimum to the geodesic one.

where \mathbf{R}_x , \mathbf{R}_y and \mathbf{R}_z are the standard 3D rotation matrices around the respective axis. As a result, indicating with c the cos and with s the sin of an angle, matrix \mathbf{R} is computed

as:

$$\mathbf{R} = \begin{bmatrix} R_{00} & R_{01} & R_{02} \\ R_{10} & R_{11} & R_{12} \\ R_{20} & R_{21} & R_{22} \end{bmatrix} = \mathbf{R}_x(\Delta\phi) \mathbf{R}_y(\Delta\theta) \mathbf{R}_z(\Delta\psi) = \begin{bmatrix} c\Delta\theta c\Delta\psi & -c\Delta\theta s\Delta\psi & s\Delta\theta \\ m & n & -c\Delta\theta s\Delta\phi \\ p & q & c\Delta\theta c\Delta\phi \end{bmatrix} \quad (30)$$

where

$$\begin{aligned} m &= c\Delta\phi s\Delta\psi + s\Delta\phi c\Delta\psi s\Delta\theta \\ n &= c\Delta\phi c\Delta\psi - s\Delta\phi s\Delta\theta s\Delta\psi \\ p &= s\Delta\phi s\Delta\psi - c\Delta\phi c\Delta\psi s\Delta\theta \\ q &= s\Delta\phi c\Delta\psi + c\Delta\phi s\Delta\theta s\Delta\psi \end{aligned}$$

Given this, with the function $t2v$ we have to perform the inverse process, retrieving the Euler angles $\Delta\phi$, $\Delta\theta$ and $\Delta\psi$ from Eq. (30). As a consequence of this, the Jacobians $\tilde{\mathbf{J}}_i$ and $\tilde{\mathbf{J}}_j$ computed through Eq. (12) and Eq. (13) are really complex and full of non-linear components.

b) Alternative Formalization: In this case, we do not use the $t2v$ function in the \boxplus , but the difference between two isometries is computed according to Eq. (26). Given the error function in Eq. (27), applying a small state perturbation $\Delta\mathbf{x}$, it will become:

$$\begin{aligned} \mathbf{e}_{ij}(\mathbf{X}_i \boxplus \Delta\mathbf{x}_i, \mathbf{X}_j \boxplus \Delta\mathbf{x}_j) &= \\ &= \text{flatten} \left((v2t(\Delta\mathbf{x}_i)\mathbf{X}_i)^{-1} (v2t(\Delta\mathbf{x}_j)\mathbf{X}_j) \right) - \text{flatten}(\mathbf{Z}_{ij}) \end{aligned} \quad (31)$$

The Jacobian $\tilde{\mathbf{J}}_j$ is computed performing the partial derivative of Eq. (31) w.r.t. $\Delta\mathbf{x}_j$:

$$\tilde{\mathbf{J}}_j = \left. \frac{\partial \mathbf{e}_{ij}(\mathbf{X}_i \boxplus \Delta\mathbf{x}_i, \mathbf{X}_j \boxplus \Delta\mathbf{x}_j)}{\partial \Delta\mathbf{x}_j} \right|_{\substack{\Delta\mathbf{x}_i = 0 \\ \Delta\mathbf{x}_j = 0}} \quad (32)$$

Therefore, we define the following matrices:

$$\mathbf{A} = \begin{bmatrix} \mathbf{R}_i^T & -\mathbf{R}_i^T \mathbf{t}_i \\ \mathbf{0} & 1 \end{bmatrix} \quad (33)$$

$$\mathbf{B} = \begin{bmatrix} (\mathbf{R}_{\Delta\mathbf{x}_i}^x \mathbf{R}_{\Delta\mathbf{x}_i}^y \mathbf{R}_{\Delta\mathbf{x}_i}^z)^T & -\mathbf{R}_{\Delta\mathbf{x}_i}^T \mathbf{t}_i \\ \mathbf{0} & 1 \end{bmatrix} \quad (34)$$

$$\mathbf{C} = \begin{bmatrix} \mathbf{R}_j & \mathbf{t}_j \\ \mathbf{0} & 1 \end{bmatrix} \quad (35)$$

where:

- \mathbf{R}'_{x0} , \mathbf{R}'_{y0} and \mathbf{R}'_{z0} that represent derivatives with respect to $\Delta\phi$, $\Delta\theta$ and $\Delta\psi$ of the base rotation $\mathbf{R}_k(\cdot)$, evaluated in 0 and with $k = \{x, y, z\}$;
- $\hat{\mathbf{R}}'_{x0}$, $\hat{\mathbf{R}}'_{y0}$, and $\hat{\mathbf{R}}'_{z0}$ that are the derivatives with respect to $\Delta\phi$, $\Delta\theta$ and $\Delta\psi$ of the rotational part of matrix \mathbf{G} , computed as $\hat{\mathbf{R}}'_{k0} = \mathbf{R}_i^T \mathbf{R}'_{k0} \mathbf{R}_j$ with $k = \{x, y, z\}$;

We indicate with $\hat{\mathbf{r}}'_{k0}$ the 9 vector obtained stacking the columns of $\hat{\mathbf{R}}'_{k0}$ - with $k = \{x, y, z\}$, and, as a result, the

Jacobian becomes:

$$\begin{aligned} \tilde{\mathbf{J}}_j &= \left. \frac{\partial [\text{flatten}(\mathbf{ABC})]}{\partial \Delta\mathbf{x}_j} \right|_{\substack{\Delta\mathbf{x}_i = 0 \\ \Delta\mathbf{x}_j = 0}} \\ &= \left(\mathbf{0}_{(9 \times 3)} \quad \left[\hat{\mathbf{r}}'_{x0} \mid \hat{\mathbf{r}}'_{y0} \mid \hat{\mathbf{r}}'_{z0} \right]_{(9 \times 3)} \right) \begin{bmatrix} \mathbf{R}_i^T & \\ & -\mathbf{R}_i^T [\mathbf{t}_j]_{\times} \end{bmatrix} \end{aligned} \quad (36)$$

Finally, $\tilde{\mathbf{J}}_i$ can be computed straightforwardly from Eq. (36), leading to the relation

$$\tilde{\mathbf{J}}_i = -\tilde{\mathbf{J}}_j$$

REFERENCES

- [1] Sameer Agarwal, Keir Mierle, and Others. Ceres solver. <http://ceres-solver.org>. 1, 2
- [2] L. Carlone, R. Aragues, J.A. Castellanos, and B. Bona. A linear approximation for graph-based simultaneous localization and mapping. In *Proc. of Robotics: Science and Systems (RSS)*, pages 41–48, 2011. 1
- [3] Luca Carlone, Roberto Tron, Kostas Daniilidis, and Frank Dellaert. Initialization techniques for 3d slam: a survey on rotation estimation and its use in pose graph optimization. In *Robotics and Automation (ICRA), 2015 IEEE International Conference on*, pages 4597–4604. IEEE, 2015. 1, 2, 5
- [4] Frank Dellaert. Factor graphs and gtsam: A hands-on introduction. Technical report, Georgia Institute of Technology, 2012. 1, 2
- [5] Frank Dellaert and Michael Kaess. Square root sam: Simultaneous localization and mapping via square root information smoothing. *The International Journal of Robotics Research*, 25(12):1181–1203, 2006. 2
- [6] T. Duckett, S. Marsland, and J. Shapiro. Fast, on-line learning of globally consistent maps. *Autonomous Robots*, 12(3):287–300, 2002. 2
- [7] U. Frese, P. Larsson, and T. Duckett. A multilevel relaxation algorithm for simultaneous localisation and mapping. *IEEE Transactions on Robotics*, 21(2):1–12, 2005. 2
- [8] G. Grisetti, R. Kümmerle, and K. Ni. Robust optimization of factor graphs by using condensed measurements. In *Proc. of the IEEE/RSJ Int. Conf. on Intelligent Robots and Systems (IROS)*, Vilamoura, Portugal, October 2012. 2
- [9] Giorgio Grisetti, Rainer Kummerle, Cyrill Stachniss, and Wolfram Burgard. A tutorial on graph-based slam. *IEEE Intelligent Transportation Systems Magazine*, 2(4):31–43, 2010. 1, 3
- [10] Giorgio Grisetti, Cyrill Stachniss, Slawomir Grzonka, and Wolfram Burgard. A tree parameterization for efficiently computing maximum likelihood maps using gradient descent. In *Robotics: Science and Systems*, volume 3, page 9, 2007. 2
- [11] J-S Gutmann and Kurt Konolige. Incremental mapping of large cyclic environments. In *Computational Intelligence in Robotics and Automation, 1999. CIRA'99. Proceedings. 1999 IEEE International Symposium on*, pages 318–325. IEEE, 1999. 2
- [12] Christoph Hertzberg, René Wagner, and Udo Frese. Tutorial on quick and easy model fitting using the slam framework. In *International Conference on Spatial Cognition*, pages 128–142. Springer, 2012. 3
- [13] A. Howard, M.J. Matarić, and G. Sukhatme. Relaxation on a mesh: a formalism for generalized localization. In *Proc. of the IEEE/RSJ Int. Conf. on Intelligent Robots and Systems (IROS)*, 2001. 2
- [14] Michael Kaess, Hordur Johannsson, Richard Roberts, Viorela Ila, John J Leonard, and Frank Dellaert. isam2: Incremental smoothing and mapping using the bayes tree. *The International Journal of Robotics Research*, 31(2):216–235, 2012. 2
- [15] Michael Kaess, Ananth Ranganathan, and Frank Dellaert. isam: Fast incremental smoothing and mapping with efficient data association. In *Robotics and Automation, 2007 IEEE International Conference on*, pages 1670–1677. IEEE, 2007. 2
- [16] Rainer Kümmerle, Giorgio Grisetti, Hauke Strasdat, Kurt Konolige, and Wolfram Burgard. g 2 o: A general framework for graph optimization. In *Robotics and Automation (ICRA), 2011 IEEE International Conference on*, pages 3607–3613. IEEE, 2011. 1, 2

- [17] Feng Lu and Evangelos Milios. Globally consistent range scan alignment for environment mapping. *Autonomous robots*, 4(4):333–349, 1997. [2](#)
- [18] Kai Ni, Drew Steedly, and Frank Dellaert. Tectonic sam: Exact, out-of-core, submap-based slam. In *Proc. of the IEEE Int. Conf. on Robotics & Automation (ICRA)*, 2007. [2](#)
- [19] Edwin Olson, John Leonard, and Seth Teller. Fast iterative alignment of pose graphs with poor initial estimates. In *Robotics and Automation, 2006. ICRA 2006. Proceedings 2006 IEEE International Conference on*, pages 2262–2269. IEEE, 2006. [2](#)
- [20] R. Smith, M. Self, and P. Cheeseman. Estimating uncertain spatial relationships in robotics. In I. Cox and G. Wilfong, editors, *Autonomous Robot Vehicles*, pages 167–193. Springer Verlag, 1990. [3](#)